Materials Science & Engineering A 765 (2019) 138304

Contents lists available at ScienceDirect

Materials Science & Engineering A

journal homepage: www.elsevier.com/locate/msea

# Reduction of shear localization through structural rejuvenation in Zr–Cu–Al bulk metallic glass

F. Meng[a,*], K. Tsuchiya[b], M.J. Kramer[c], R.T. Ott[c]

[a] Sino-French Institute of Nuclear Engineering and Technology, Sun Yat-Sen University, Zhuhai, Guangdong, 519082, China
[b] International Center for Young Scientist, National Institute for Materials Science, Sengen 1-2-1, Tsukuba, Ibaraki, 305-0047, Japan
[c] Division of Materials Science and Engineering, Ames Laboratory (USDOE), Ames, IA, 50010, USA

ARTICLE INFO

*Keywords:*
Severe plastic deformation
Structural rejuvenation
Metallic glass
Pair distribution function
Nanoindentation

ABSTRACT

The effect of high-pressure torsion (HPT) on the structure and mechanical behavior of $Zr_{50}Cu_{40}Al_{10}$ bulk metallic glass was investigated using calorimetry, density measurement, high-energy X-ray scattering and nanoindentation. Increase in rotation number, and thus plastic deformation, lowers the hardness and elastic modulus, as well as the critical strain rate for suppressing the shear localization. Strain-softening induced by plastic deformation is attributed to the structural rejuvenation. Wide-angle X-ray scattering (WAXS) measurements suggest that HPT deformation reduces and broadens the peaks in the pair distribution function indicative of pronounced structural disordering and enabling structural rejuvenation. Measured excess free volume of 0.8% for samples deformed by HPT with a maximum structural relaxation enthalpy of 29.5 J/g in the sample with 20 and 50 revolutions.

## 1. Introduction

Plastic deformation in glassy metals at room temperature has been described using many types of models including the free volume [1], shear transformation zone [2]. Over a large-range of strain rates, plastic deformation in metallic glasses is localized in thin shear bands, which significantly limit macroscopic ductility [3,4]. Restricting the nucleation and propagation of shear bands is regarded as an effective way to improve the room temperature plasticity. Introduction of residual stress [5], nanocrystalline particles [6] or microstructural heterogeneity [7] have been shown to be effective methods in restricting the propagation of shear bands. At the atomic scale, accommodation of shear strain in metallic glass under an applied stress is believed to occur *via* local re-arrangement of atoms around free volume region. The cluster of atoms that undergoes rearrangement is referred to as the shear transformation zone (STZ) [4]. Since STZs are thought to involve re-arrangements of clusters of atoms, most studies typically rely on MD simulations of plastic flow in glassy metals [8]. To validate these models, we need experimental observations of the structural and mechanical property interconnections associated with plastic flow in amorphous metals.

Recently, high-pressure torsion (HPT) deformation of coin-shaped sample by compressive force and torsion straining [9], has become a widely-used technique for imparting large plastic strains in brittle alloys and intermetallic compounds. Since extensive strain can be applied by simply increasing the number of rotations, this technique has become popular for grain refinement [10], and to fabricate composite amorphous structures through crystalline-to-amorphous transformation [9,11]. The HPT straining is believed to modify the structures of metallic glasses by increasing their free volume and inducing microstructural heterogeneity at nanoscale through deformation-induced atomic disordering processes [12].

Previous studies have also demonstrated that HPT deformation in the $Zr_{50}Cu_{40}Al_{10}$ metallic glass reduced the elastic modulus and hardness, which is associated with the deformation mode transitioning from inhomogeneous shear localization to homogeneous plastic deformation at a critical loading rate [13]. However, the dependence of deformation mechanism on the strain rate after structural rejuvenation is not fully understood and the rejuvenated volume has not been quantitatively measured. In the present study, density and Differential Scanning Calorimetry (DSC) measurements were carried out to quantify the physical and thermodynamic properties of HPT deformed samples to correlate them with the mechanical properties measured *via* nanoindentation. The structural evolution and mechanism for strain-softening and reduction of shear localization are discussed.

## 2. Experimental procedure

A ϕ10 mm cylindrical ingot of $Zr_{50}Cu_{40}Al_{10}$ was prepared by the

* Corresponding author.
*E-mail address:* mengfq5@mail.sysu.edu.cn (F. Meng).

https://doi.org/10.1016/j.msea.2019.138304
Received 21 July 2019; Received in revised form 13 August 2019; Accepted 17 August 2019
Available online 18 August 2019
0921-5093/ 

tilt-casting method [13]. Disks of 0.85 mm thickness were sliced from the as-cast rod and then subjected to HPT deformation using quasi-constrained-geometry anvils (tool steel YXR3, Hitachi Metals Tool Steel, Ltd., Japan) under a compressive pressure of 5 GPa at room temperature for various numbers of rotation with a rotation speed of 1 rpm. The number of rotations, $N$, were chosen as 1, 10, 20 and 50, which correspond to the equivalent von Mises strains of 17, 170, 341 and 853, respectively, at a position 4 mm from the center of the disk. The mechanical properties before and after deformation were characterized by nanoindentation using a Hysitron Tribo-indenter TI950 in load and displacement control modes. In load control mode, different loading rates of 25, 250 and 2500 μN/s were performed while the maximum load is kept at 5000 μN. The elastic modulus and hardness were calculated by the Oliver and Pharr method [14] for each sample. Samples for the nanoindentation test were mechanically polished to a mirror-like surface using $SiO_2$ colloidal suspension (0.06 μm) as the final step. The nanoindentation measurements was taken at an area 4 mm away from the center of the disk in cross section.

High energy x-ray scattering was performed at the beamline 11-ID-B of the Advanced Photon Source, Argonne National Laboratory. The incident energy was 86.7 keV and the beam size was 0.5 × 0.5 $mm^2$. More details about synchrotron work are described elsewhere [15]. Reduced pair distribution functions were calculated using PDFgetX2 package [16]. Density measurement was performed at room temperature by the Archimedes method with a Mettler Toledo AX26 electrical balance with a sensitivity of 2 μg. Three discs with total mass of ~1.2 g were prepared for density measurement at each condition. Thermal analysis of HPT-deformed disks was performed using a Perkin-Elmer Diamond Differential Scanning Calorimeter with a heating/cooling rate of 0.667 K/s under a nitrogen atmosphere. The samples for the DSC measurement were cut from the edge of the disk by including the region for the nanoindentation test with mass ~30 mg. The samples used for measuring relaxation enthalpy were heated up to 873 K twice with secondary heating cycle used as baseline.

## 3. Results

### 3.1. Strain-softening

The Young's modulus ($E$) and hardness ($H$) as a function of rotation number ($N$) and equivalent strain (ε) determined from the nanoindentation tests at a loading rate of 250 μN/s are plotted in Fig. 1. Increasing the rotation number, and thus equivalent strain, leads to a clear decrease in both $E$ and $H$. The reduction of $H$ is consistent with strain-softening induced by HPT deformation. Interestingly, annealing

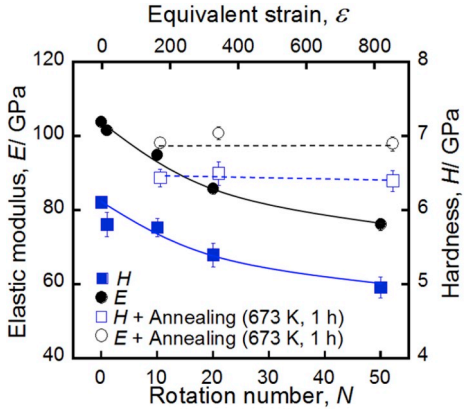


**Fig. 1.** Dependence of elastic modulus ($E$) and hardness ($H$) obtained at the position 4 mm from the center of the disk on the rotation number and equivalent strain. As-cast sample is plotted as $N = 0$. Open symbols denote the data obtained from samples with $N = 10$, 20 and 50 after structural relaxation at 673 K for 1 h. All data were obtained at a loading rate of 250 μN/s.

the HPT deformed samples at 673 K for 1 h leads to a recovery of modulus slightly below the as cast value, while the hardness shows an increase beyond the as cast value, Fig. 1 (open symbols). Furthermore, $E$ and $H$ show almost same values after annealing in the sample deformed with $N = 10$, 20 and 50, suggesting that the structural state after annealing at 673 K is similar for all the samples.

### 3.2. Shear localizations

Previous studies [13] have shown that torsional straining not only reduces the $E$ and $H$ (Fig. 1) in $Zr_{50}Cu_{40}Al_{10}$ BMG, but also suppresses shear localization at loading rate of 250 μN/s. Fig. 2 show the representative loading curves at different loading rates in the as-cast and deformed samples. Inset SPM images shown in Fig. 2a–d clearly demonstrates that the number of shear bands around indents is suppressed by increasing HPT revolutions at a same loading rate of 250 μN/s. The sample deformed by HPT for 50 revolutions, Fig. 2d, does not deform by shear localization but rather homogeneous flow during nanoindentation testing at a loading rate of 250 μN/s.

It has been widely known that the shear localization is not only dependent on the chemical composition of samples, but also the loading conditions, such as strain rate [17,18]. In order to clarify the effect of severe plastic deformation on the shear localization of bulk metallic glass, nanoindentation with other loading rates, 25 μN/s and 2500 μN/s, were performed and the typical loading segment are shown in Fig. 2a–d. The different curves have been offset along the displacement axis for clarity. The maximum depth after loading segment at a loading rate of 250 μN/s is denoted in each of the plots. The increase in the maximum depth with increasing HPT rotations suggests the mechanical softening is induced by the torsional straining, in agreement with the reduction of $E$ and $H$. The loading curves shown in Fig. 2a–c clearly show discontinuities, or "pop-ins", in which the depth increases at an approximately constant load. In crystalline materials, these discontinuities are typically associated with discrete plastic deformation or dislocation nucleation [19]. In amorphous materials, they are likened to the serrated flow correlated to the nucleation and propagation of shear bands [20]. It is interesting to note that the increase in rotation number reduces the number of serrations at the same loading rate and the loading curves become smoother, suggesting the shear localization was suppressed by HPT.

The nature of the serrations or "pop-in" depends on the loading rate where slow loading conditions appear to promote the occurrence of serrations and higher loading rates decrease the number of serrations. For example, as-cast metallic glass shown in Fig. 2a, the number of serrations markedly increases as the loading rate decreases from 2500 to 25 μN/s. Similar phenomena are present in HPT deformed sample with $N = 10$ and 20, Fig. 2b and c. For the HPT deformed sample with $N = 50$, smooth loading curves without visible serration can be observed at loading rates of 250 and 2500 μN/s. However, several pop-in events appear at loading rate of 25 μN/s, suggesting the deformation mechanics at lower loading rate of 25 μN/s is still *via* shear localization in the deformed sample with $N = 50$. The increase in the serrations with the reducing loading rate has been found in tensile and compressive stress-strain curves of other BMGs [17,18,21]. In the present study, appearance of pop-in events at lowest loading rate also suggests that the critical strain rate for activating shear localization is reduced by HPT.

Schuh et al. correlated this phenomena with a single big shear band that may operate to swiftly accommodate applied shear strain in the slower strain rate, while at high strain rates multiple shear bands with smaller shear offset are involved to accommodate the strain [22]. A method to evaluate the strain rate sensitivity of serrated flow based on the nanoindentation curves was proposed by Schuh et al. [22]. During nanoindentation with constant loading rate in Fig. 2, the displacement (Depth) rate is a non-linear function of time, as is the indentation strain rate, which is defined as [22,23]:

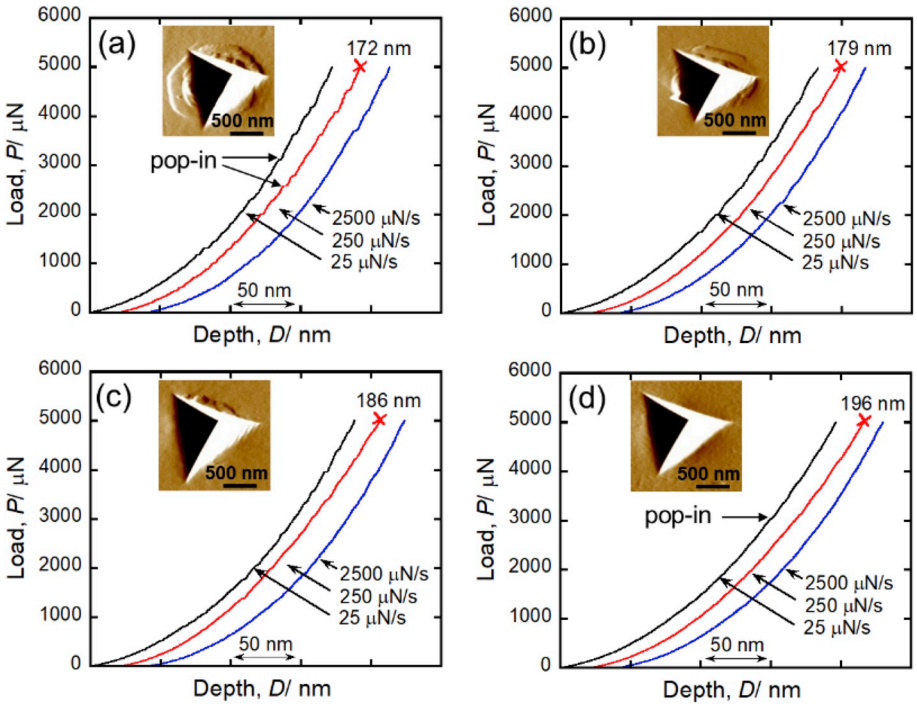


**Fig. 2.** The loading segments of the load-depth curves under different loading rates and corresponding SPM images of the indents at a loading rate of 250 μN/s in the (a) as-cast and HPT deformed samples with (b) $N = 10$, (c) $N = 20$ and (d) $N = 50$. The maximum depths at the loading segment with a loading rate of 250 μN/s are traced in each sample.

$$\dot{\varepsilon} = \frac{1}{D}\frac{dD}{dt} \tag{1}$$

where $t$ is time, $D$ is the indentation depth. In Fig. 3, the calculated strain rate under different loading rates is plotted as a function of depth for the samples before and after HPT deformation with different rotation numbers. Although the strain rate decreases throughout the test history, the trend is not smooth but is punctuated by many short bursts or peaks to higher strain rates, representing a short period during which the indenter tip sinks quickly into the specimen. All the peaks shown in Fig. 3 can be exactly correlated to the serrations observed in the loading portions shown in Fig. 2. The number and height of these peaks become fewer and shorter in the same sample indented at higher loading rate.

A clear tendency is observed where the serrations become less prominent with higher loading rate and rotation number in Figs. 2 and 3. This trend can be quantified by considering the normalized height $A$ of the serrated peaks, defined as [22,23]:

$$A = \frac{\dot{\varepsilon}_{max}}{\dot{\varepsilon}} \tag{2}$$

where $\dot{\varepsilon}_{max}$ is the maximum strain rate measured at the tip of the peak, and the $\dot{\varepsilon}$ is the average background strain rate surrounding the peak. The normalized $A$ thus represents the factor by which the deformation is accelerated during the pop-in event. Fig. 4 shows the dependence of $A$ on the indentation strain rate in the different samples. Although the scatter in the data is significant, it highlights the trend shown in Figs. 2

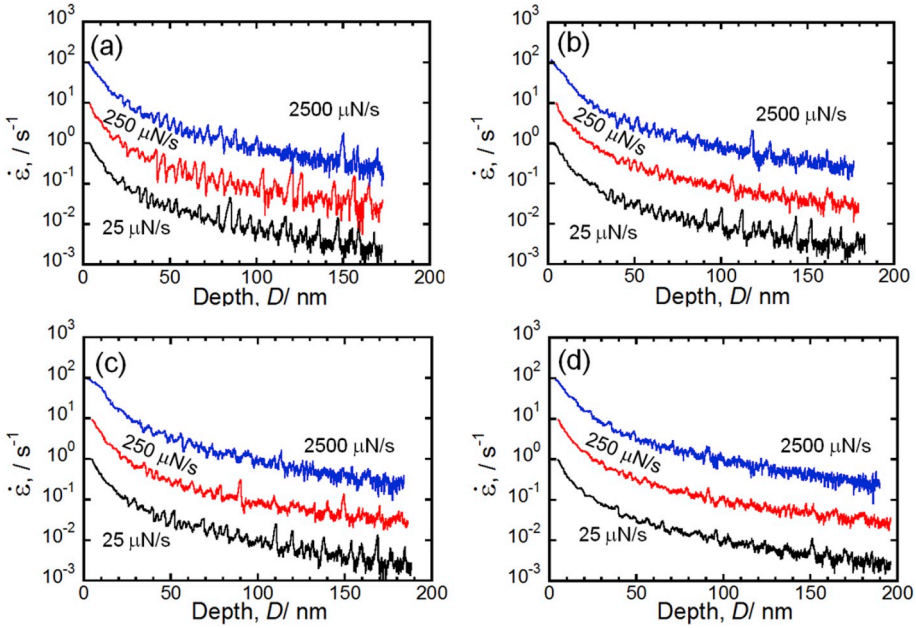


**Fig. 3.** The indentation strain rate plotted as a function of the indentation depth for (a) as-cast and HPT deformed samples with (b) $N = 10$, (c) $N = 20$ and (d) $N = 50$.

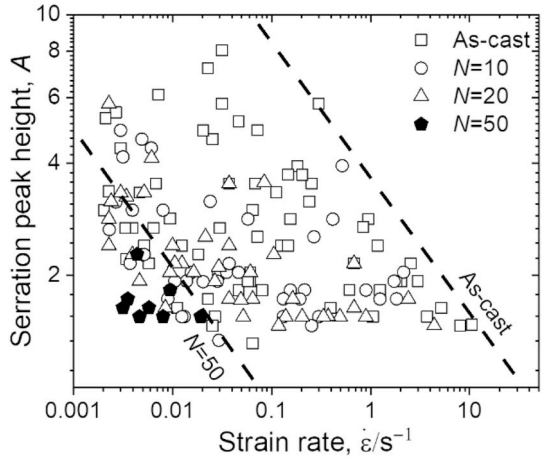


**Fig. 4.** The dependence of normalized height $A$ on the indentation strain rate in the different samples; dash line marked the critical strain rate to suppress shear localization in as-cast and $N = 50$ samples.

and 3, illustrating a decrease in the prominence of serrations with increasing HPT deformation. All the points measured in the sample deformed with $N = 20$ and 50 concentrates in the lower strain rate and lower $A$ compared to these in the as-cast sample, indicating the serrations can still occur in the deformed sample with $N = 50$ when the indentation is performed at a lower loading rate, but with smaller burst of depth. Furthermore, an increase in strain rate invariably reduced the measured normalized height ($A$), and above the threshold strain rate, the serration peaks are no longer observed, resulting in absence of visible shear localization. Critical strain rate, above which the serrated plastic deformation can be suppressed, can also be reflected in the figure of normalized height dependence on the strain rate. Two dash lines marks the critical strain rate to suppress the shear localization in as-cast and $N = 50$ samples. HPT deformation reduces the critical strain rate of suppressing shear localizations from 10 $s^{-1}$ in as-cast to 0.1 $s^{-1}$ after 50 revolutions. The critical strain rate in the sample with $N = 50$ is two order of magnitude lower than it in as-cast one (10 $s^{-1}$). It is important to note that although the indentation strain rate is qualitatively useful, the critical strain rate estimated by indentation is usually 10 times greater than equivalent, uniaxial strain rate [24].

### 3.3. Structural rejuvenation

Reduction of hardness after HPT deformations believed to correspond changes in the local atomic structure via rejuvenation. To determine the magnitude of rejuvenated volume, the thermal properties of the samples before and after HPT deformation with different number of rotations were investigated by DSC with a heating rate of 0.667 K/s, Fig. 5a. The presence of glass transition and crystallization in the as-cast and deformed samples is additional evidence that the HPT deformed samples remain amorphous, which has been confirmed by transmission electron microscope observations (Fig. S1 in Supplementary Materials). Additionally, there is a broad exothermic peak over wide temperature range from ~380-700 K before the glass transition in the deformed samples (inset of Fig. 5a), which is related to thermally induced structural relaxation, *i.e.* annihilation of free and anti-free volume, as well as the rearrangement of short-range ordering atomic clusters [25,26]. The different degrees structural relaxation is believed to be directly related to the free volume creation and structural disordering created by HPT deformation of the samples [27]. Increasing the HPT deformation up to a rotation number up to 20 leads to a pronounced increase in the exothermic heat release before $T_g$. However, with continued deformation up to $N = 50$, the exothermic heat release does not increase significantly. The difference between the integrated area of the exotherms between the deformed sample and the as-cast sample at the temperature below $T_g$ is referred to as the relaxation enthalpy, which is proportional to the amount of rejuvenated volume and extent of disordering introduced by deformation [28]. The calculated relaxation enthalpy is plotted in Fig. 5b as a function of rotation number. An increase in rotation number leads to a higher relaxation enthalpy, until reaching saturation as $N > 20$.

The increase in the rejuvenated volume can also be characterized by the density change at the room temperature for samples before and after HPT deformation, Fig. 5c. Similar to the magnitude of change in the enthalpy of relaxation, the magnitude of the density change is quite significant for samples deformed up to rotation number ($N$) of 20. With increasing rotation number higher than 20, the density does not exhibit a significant change, which also is consistent with the enthalpy of relaxation behavior, Fig. 5b. If the decrease in density in the deformed samples is assumed to characteristic of an increase in the free volume, the free volume change, $\Delta v$, for the HPT deformed samples can be calculated according to the equation proposed by Haruyama et al. [29].

$$\Delta v = \frac{v_f}{\gamma v^*} = \frac{2(\rho_0 - \rho_N)}{\rho_0} \tag{3}$$

where the $v^*$ is the critical value of free volume for atomic diffusion, $v_f$ is the average free volume per atom, $r$ is the correction term for overlap of free volume, $\rho_0$ is the density of as-cast sample and $\rho_N$ is the density of the sample after HPT deformation with $N$ revolutions. The calculated free volume change is plotted in Fig. 5c as a function of rotation number with solid square symbols. Since the change in free volume is calculated from the change in the bulk density, their dependence on the amount of plastic strain (i.e., number of rotations during HPT) is the same, albeit, opposite in sign. The maximum increase in free volume change is about 0.89%, obtained in the samples with $N = 20$ and 50. Assuming that the quenched-in free volume in the as-cast alloys is 0.8% [30], the maximum free volume is ~1.69% in the samples with $N = 20$ and 50, which is higher than in the center of a shear band [31].

The relaxation of the rejuvenated volume in the sample with $N = 50$

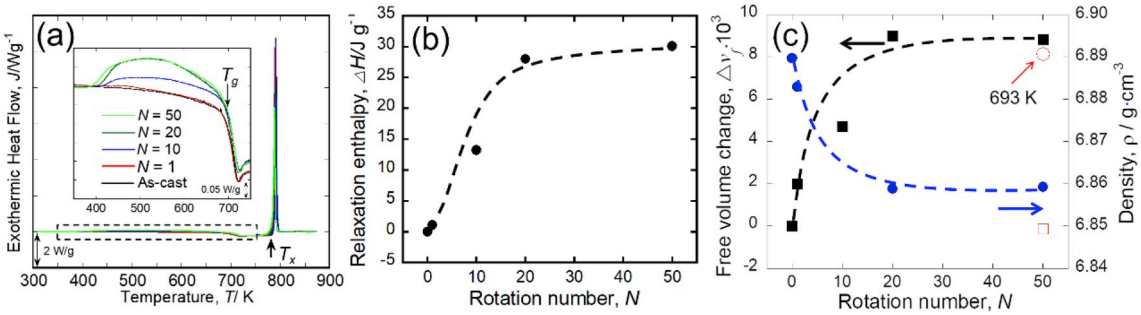


**Fig. 5.** (a) DSC curves in the samples before and after HPT deformation with different number of rotations. The inset shows enlargement of the area marked by a dashed rectangle; (b) dependence of relaxation enthalpy on the rotation number, (c) the dependence of density (solid circle symbol) and free volume change (solid square symbol) on the rotation number. The open circle and square symbols denote the density and free volume change in the sample annealed at 693 K for 1000 s.

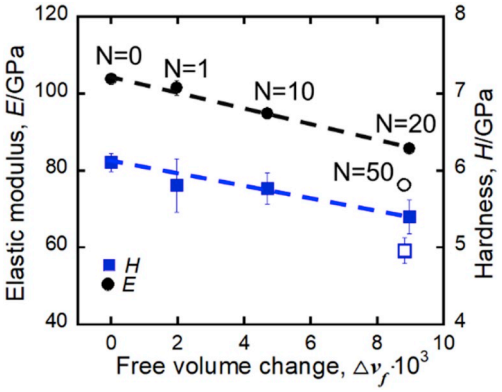


**Fig. 6.** Evolution of elastic modulus ($E$) and hardness ($H$) obtained at a loading rate of 250 μN/s as a function of the free volume change in the as-cast and HPT deformed samples.

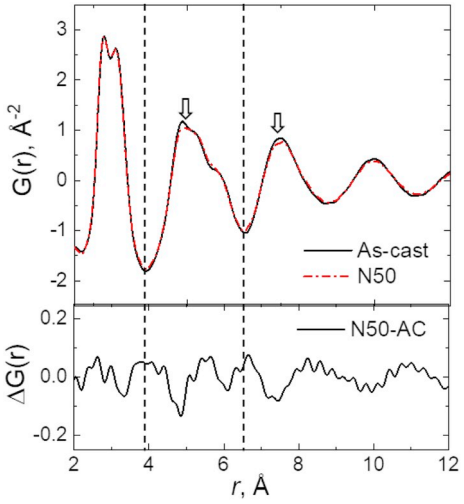


**Fig. 7.** (upper) the RPDF (G(r)) profiles of as-cast and deformed with $N = 50$ (N50); (bottom) the difference (ΔG(r)) between deformed and as-cast samples.

was carried out by annealing at 693 K for 1000 s. The density and free volume change after relaxation, open symbols in Fig. 5c, show that the relaxed sample density is slightly higher than as-cast sample, suggesting that the relaxation has annihilated the free volume that was created by the plastic deformation via HPT as well as excess free volume "frozen in" during casting. TEM observations (not shown) reveal that no crystallization occurs in the sample after relaxation at 693 K for 1000 s, highlighting that the density change appears to be caused only by the annihilation of rejuvenated structure and not by crystallization. The recovery of density after structural relaxation also excludes the density change being caused by nanovoids and/or cracks during deformation.

To further characterize the dependence of the mechanical properties of the deformed samples on the structural changes, both $E$ and $H$ (measured at a loading rate of 250 μN/s) were correlated with the free volume change calculated from the density changes, Fig. 6. Both $E$ and $H$ show a linear decrease with increasing free volume change, with the exception of the samples deformed $N = 50$ (open symbols). Although the free volume changes in the sample with $N = 20$ and 50 show similar values, both $E$ and $H$ are substantially different. The deviation from the linear relationship between free volume change and $E$ and $H$ in the sample with $N = 50$ suggests that the strain-softening is not only caused by the free volume change, but also by other kinds of "defects".

Both relaxation enthalpy and density measurement demonstrate that HPT introduces more rejuvenated volume into glassy matrix and resulting in the strain-softening. To investigate the effects of the HPT on the atomic structure more closely, wide-angle X-ray scattering (WAXS) was performed to obtain reduced pair distribution functions (RPDF) for the as-cast and deformed samples with $N = 50$, Fig. 7. For the HPT deformed sample, the RPDF peak positions do not appear to show any obvious shifts compared to those of the as-cast sample, however, the peak heights of the RPDF (marked by arrows) for the deformed sample appear to be reduced, especially at larger $r$. Furthermore, the minima in the RPDF (marked dash lines) are enhanced after HPT, as clearly seen in difference (ΔG(r)) plot Fig. 7. It is interesting to note that intensity of the first coordination shell shows the least change for the different shells.

## 4. Discussion

Owing to absence of dislocation-mediated crystallographic slip in BMGs, activation of the rearrangement of a particular oriented cluster of atoms, known as shear transformation zone (STZ), mediates the deformation to accommodate applied strain [4]. DSC analysis and density measurements, as well as RPDF measurements, have demonstrated that HPT deformation introduces a measurable amount of rejuvenated volume into the BMG, such as free and anti-free volumes. It is known that local atomic environments around rejuvenated structure site (i.e. free volume) have very low shear modulus and can be shifted with minimal energy cost. Thus, they can be referred to as "defects" and are potential sites to become STZs under an applied stress. In the HPT deformed samples with higher rotation numbers, the high amount of rejuvenated volume disorders the local atomic structure, which causes a decrease in the strength, which can be supported by the linear correlation between $H$ and free volume change as shown in Fig. 6.

The fundamental unit of plasticity during inhomogeneous deformation of BMGs can be the STZ, which is preferentially nucleated at rejuvenated site. The continued propagation of applied shear strain occurs when one STZ creates a localized distortion of the surrounding materials, which triggers the formation of large planar bands of STZs, or so-called "shear bands" [32,33]. In the nanoindentation test, the distribution of stress field around the indenter drives the spatial propagation of small displacement by the chaining of many STZ in sequence, and leads to the serrated plastic flow in the load-depth curves [33].

In the as-cast sample, there is insufficient rejuvenated volume; hence new rejuvenated volume has to be created most likely at the shear front in an auto-catalystic manner under the acting shear stress. The propagation of STZ follows the shear stress around the indenter. Finally, a large planar band of STZ called "shear band event" is formed, and some of them propagate to the surface causing surface step and pileups as shown in the SPM images (Fig. 2). Uniform distribution of large amount of rejuvenated volume in the sample with $N = 50$ leads to homogeneous distribution of strain but not localized around indenter, which leads to the transformation of deformation modes from shear localization to homogeneity at loading rate of 250 μN/s and 2500 μN/s. The observed reduction of shear localization and strain-softening are consistent with the MD simulation of nanoindentation of metallic glass by Shi and Falk [34].

As shown in Fig. 4, the normalized height $A$ measured from the as-cast and deformed samples at different loading rates becomes smaller and shifts to lower strain rate after HPT deformation, suggesting the critical strain rate for suppressing the shear localization at room temperature is reduced by HPT deformation. For the HPT deformed sample with $N = 50$, there is almost no serrations observed in the loading segment for rates of 250 and 2500 μN/s, while few serrated flow occur for the lower loading rate of 25 μN/s. The appearance of serration at lower loading rates can be explained by the crossover in the applied strain rate and the frequency of STZ formation. The stress induced by the distortion at the front of the STZ triggers atomic rearrangement that yield enhanced local ordering, which leads to the shear localization again.

## 5. Summary

Deformation mechanisms of $Zr_{50}Cu_{40}Al_{10}$ BMG before and after structural rejuvenation were investigated using nanoindentation. Shear localization events were significantly reduced after rejuvenation with the critical strain rate to active shear serrated flows lowered by 2 orders of magnitude after 50 revolutions compared to the as-cast condition. The high amount of rejuvenated volume introduced by HPT deformation disperses the shear location, resulting in reduction of pop-in events. An increase in free volume leads to the linear decrease in the elastic modulus and hardness with the maximum free volume introduced by high pressure torsion is saturated at 0.89% after 20 revolutions.

## Acknowledgement

The authors thank Yoshihiko Yokoyama (Institute of Metal Research, Tohoku University) for providing amorphous ingots. This work was supported by Ames Laboratory the U.S. Department of Energy, Office of Science, Basic Energy Sciences, Materials Science and Engineering Division. Ames Laboratory is operated for the U.S. Department of Energy by Iowa State University under Contract No. DE-AC02-07CH11358. The use of the Advanced Photon Source was supported by the US Department of Energy, Office of Science, Office of Basic Energy Sciences, under Contract No. DE-AC02-06CH11357.

## Appendix A. Supplementary data

Supplementary data to this article can be found online at https://doi.org/10.1016/j.msea.2019.138304.

## References

[1] F. Spaepen, A microscopic mechanism for steady state inhomogeneous flow in metallic glasses, Acta Metall. 25 (4) (1977) 407–415.
[2] A.S. Argon, Plastic deformation in metallic glasses, Acta Metall. 27 (1) (1979) 47–58.
[3] F. Spaepen, A microscopic mechanism for steady state inhomogeneous flow in metallic glasses, Acta Metall. 25 (1977) 407–415.
[4] A.S. Argon, Plastic deformation in metallic glasses, Acta Metall. 27 (1979) 47–58.
[5] Y. Zhang, W.H. Wang, A.L. Greer, Makingmetallic glasses plastic by control of residual stress, Nat. Mater. 5 (2006) 857–860.
[6] S. Pauly, G. Liu, G. Wang, U. Kuhn, N. Mattern, J. Eckert, Microstructural heterogeneities governing the deformation of $Cu_{47.5}Zr_{47.5}Al_5$ bulk metallic glass composites, Acta Mater. 57 (18) (2009) 5445–5453.
[7] Y.H. Liu, G. Wang, R.J. Wang, D.Q. Zhao, M.X. Pan, W.H. Wang, Super plastic bulk metallic glasses at room temperature, Science 315 (5817) (2007) 1385–1388.
[8] L. Li, E.R. Homer, C.A. Schuh, Shear transformation zone dynamics model for metallic glasses incorporating free volume as a state variable, Acta Mater. 61 (9) (2013) 3347–3359.
[9] A.P. Zhilyaev, T.G. Langdon, Using high-pressure torsion for metal processing: fundamentals and applications, Prog. Mater. Sci. 53 (6) (2008) 893–979.
[10] R.Z. Valiev, R.K. Islamgaliev, Bulk nanostructured materials from severe plastic deformation, Prog. Mater. Sci. 45 (2000) 103–189.
[11] F.Q. Meng, K. Tsuchiya, Y. Yokoyama, Crystalline to amorphous transformation in Zr-Cu-Al alloys induced by high pressure torsion, Intermetallics 37 (0) (2013) 52–58.
[12] Y.B. Wang, D.D. Qu, X.H. Wang, Y. Cao, X.Z. Liao, M. Kawasaki, S.P. Ringer, Z.W. Shan, T.G. Langdon, J. Shen, Introducing a strain-hardening capability to improve the ductility of bulk metallic glasses via severe plastic deformation, Acta Mater. 60 (2012) 253–260.
[13] F.Q. Meng, K. Tsuchiya, S. Ii, Y. Yokoyama, Reversible transition of deformation mode by structural rejuvenation and relaxation in bulk metallic glass, App, Phys. Lett. 101 (12) (2012) 121914.
[14] W.C. Oliver, G.M. Pharr, An improved technique for determining hardness and elastic modulus using load and displacement sensing indentation experiments, J. Mater. Res. 7 (6) (1992) 1564–1583.
[15] W. Dmowski, Y. Yokoyama, A. Chuang, Y. Ren, M. Umemoto, K. Tsuchiya, A. Inoue, T. Egami, Structural rejuvenation in a bulk metallic glass induced by severe plastic deformation, Acta Mater. 58 (2) (2010) 429–438.
[16] X. Qiu, J.W. Thompson, S.J.L. Billinge, PDFgetX2: a GUI-driven program to obtain the pair distribution function from X-ray powder diffraction data, J. Appl. Crystallogr. 37 (4) (2004) 678-678.
[17] T. Mukai, T.G. Nieh, Y. Kawamura, A. Inoue, K. Higashi, Effect of strain rate on compressive behavior of a Pd40Ni40P20 bulk metallic glass, Intermetallics 10 (11) (2002) 1071–1077.
[18] T. Mukai, T.G. Nieh, Y. Kawamura, A. Inoue, K. Higashi, Dynamic response of a Pd40Ni40P20 bulk metallic glass in tension, Scr. Mater. 46 (1) (2002) 43–47.
[19] D.F. Bahr, D.E. Kramer, W.W. Gerberich, Non-linear deformation mechanisms during nanoindentation, Acta Mater. 46 (10) (1998) 3605–3617.
[20] Y.I. Golovin, V.I. Ivolgin, V.A. Khonik, K. Kitagawa, A.I. Tyurin, Serrated plastic flow during nanoindentation of a bulk metallic glass, Scr. Mater. 45 (8) (2001) 947–952.
[21] T. Mukai, T.G. Nieh, Y. Kawamura, A. Inoue, K. Higashi, Effect of strain rate on compressive behavior of a $Pd_{40}$ $Ni_{40}$ $P_{20}$ bulk metallic glass, Intermetallics 10 (2002) 1071–1077.
[22] C.A. Schuh, T.G. Nieh, Y. Kawamura, Rate dependence of serrated flow during nanoindentation of a bulk metallic glass, J. Mater. Res. 17 (7) (2002) 1651–1654.
[23] C.A. Schuh, T.G. Nieh, A nanoindentation study of serrated flow in bulk metallic glasses, Acta Mater. 51 (1) (2003) 87–99.
[24] W.H. Poisl, W.C. Oliver, B.D. Fabes, Relationship between indentation and uniaxial creep in amorphous selenium, J. Mater. Res. 10 (8) (1995) 2024–2032.
[25] O. Haruyama, H. Sakagami, N. Nishiyama, A. Inoue, The free volume kinetics during structural relaxation in bulk Pd-P based metallic glasses, Mater. Sci. Eng. A Struct. Mater. Prop. Microstruct. Process. 449 (2007) 497–500.
[26] H.B. Yu, R. Richert, K. Samwer, Structural rearrangements governing Johari-Goldstein relaxations in metallic glasses, Sci. Adv. 3 (11) (2017).
[27] S.V. Ketov, Y.H. Sun, S. Nachum, Z. Lu, A. Checchi, A.R. Beraldin, H.Y. Bai, W.H. Wang, D.V. Louzguine-Luzgin, M.A. Carpenter, A.L. Greer, Rejuvenation of metallic glasses by non-affine thermal strain, Nature 524 (7564) (2015) 200–203.
[28] A. Slipenyuk, J. Eckert, Correlation between enthalpy change and free volume reduction during structural relaxation of $Zr_{55}Cu_{30}Al_{10}Ni_5$ metallic glass, Scr. Mater. 50 (2004) 39–44.
[29] O. Haruyama, A. Inoue, Free volume kinetics during sub- Tg structural relaxation of a bulk $Pd_{40}Ni_{40}P_{20}$ metallic glass, App, Phys. Lett. 88 (13) (2006) 131906.
[30] R. Huang, Z. Suo, J.H. Prevost, W.D. Nix, Inhomogeneous deformation in metallic glasses, J. Mech. Phys. Solids 50 (5) (2002) 1011–1027.
[31] J. Pan, Q. Chen, L. Liu, Y. Li, Softening and dilatation in a single shear band, Acta Mater. 59 (2011) 5146–5158.
[32] M.M. Trexler, N.N. Thadhani, Mechanical properties of bulk metallic glasses, Prog. Mater. Sci. 55 (8) (2010) 759–839.
[33] C.A. Schuh, T.C. Hufnagel, U. Ramamurty, Mechanical behavior of amorphous alloys, Acta Mater. 55 (12) (2007) 4067–4109.
[34] Y. Shi, M.L. Falk, Stress-induced structural transformation and shear banding during simulated nanoindentation of a metallic glass, Acta Mater. 55 (13) (2007) 4317–4324.